Laser directed energy deposition of a high performance $(CoCrNi)_{94}(TiAl)_6$ additive part with a novel core-shell structured strengthening phase

Abstract: $(CoCrNi)_{94}(TiAl)_6$ medium-entropy alloy additive parts were fabricated by laser-directed energy deposition. The strengthening induction mechanism in the additive part was investigated by electron backscatter diffraction and transmission electron microscopy. Results show that the addition of TiAl powder led to increases of 29.6% and 34.3% for the tensile strength and yield strength (YS), respectively, at 298 K and a decrease of 17.0% for the elongation. In addition, the tensile strength, YS, and elongation increased by 26.6%, 22.1%, and 33.9%, respectively, at 77 K after TiAl powder was added. Microstructural observation results indicate that the matrix grains changed from the initial columnar grains with uniform growth direction to fine dendrites. A large number of TiO clad Al_2O_3 strengthening nano-precipitates with a novel core–shell structure were found in the additive parts, and both featured a face-centered cubic structure. No crystallographic orientation was observed between the nano-precipitates and the matrix. At 298 K, the dislocation line bypassed the nano-precipitates during the plastic deformation period, and Lomer–Cottrell locks appeared near the nano-precipitates, thereby inducing the strengthening of additive parts. At 77 K, plastic deformation resulted in a synergistic deformation of the nano-precipitates and the matrix, and the formation of large quantity of dislocations, which further increased the strength and plasticity of the additive parts.

Keywords: $(CoCrNi)_{94}(TiAl)_6$ MEA; Laser-directed energy deposition; Nano-precipitate; Dislocation; Orientation relationship

1. Introduction

High-performance structural materials for extreme cryogenic service are increasingly in demand in the modern industry. Most conventional alloys exhibit an increase in strength and a

decrease in plastic toughness as the temperature decreases. Medium-entropy alloys (MEAs) and high-entropy alloys represented a novel concept in the design of alloy materials. They have the potential to break through the limits of conventional material properties, making their application in extreme environments especially promising. The face-centered cubic (FCC) structure of CoCrNi MEA has excellent strength and fracture toughness[1, 2]. However, the relatively low yield strength (YS) of single-phase CoCrNi MEA is the main limitation for its cryogenic applications in engineering. Therefore, studying the strengthening and toughening mechanism of CoCrNi MEA has great importance for the expansion of its industrial application.

Strengthening CoCrNi MEA by adding alloying elements is a critical approach at present. Numerous studies analyzed the effect of single elements, such as Al[3-6], Mo[7-9], W[10, 11], Cu[12, 13], and Ti[14], on the microstructure and properties of MEAs. When 13 at.% Al was added to the laser-directed energy deposition (L-DED) CoCrNi matrix, the YS and ultimate tensile strength (UTS) of the $(CoCrNi)_{87}Al_{13}$ alloy improved by 67% and 59%, respectively[15]. The L-DED $(CoCrNi)_{87}Al_{13}$ alloy was composed of FCC (Co/Cr-rich) + B2 (Ni/Al-rich) + BCC (Co/Cr-rich) phases. $CoCrNiTi_{0.1}$ micro-alloyed MEA was fabricated by laser deposition, exhibiting unprecedented surface wrinkling under compression[14]. A precipitate-strengthened $Co_{31.7}Cr_{26.7}Ni_{36.7}Ti_{5.0}$ MEA with a high-density η-Ni_3Ti phase was fabricated by vacuum arc melting and cold rolling[16]. The FCC/η interface exhibited semi-coherence, adopting an interplanar angle of 23°.

The addition of two or more alloying elements, such as Mo + Ti[17], Al + Mo[7], and Al + Ti[18-20], to an MEA tends to exhibit better comprehensive properties. Superior mechanical properties with UTS of 1.6 GPa, YS of 1.2 GPa, and fracture strain of 13.1% at ambient temperature were achieved in $(CoCrNi)_{94}Ti_3Al_3$ MEA ingots prepared in a vacuum magnetic levitation melting furnace by using pure metals[20]. Rolled $(CoCrNi)_{100-2x}(AlTi)_x$ (x = 3, 5, and 7 at.%) alloys at 873–1173 K were systematically investigated[21]. $(CoCrNi)_{100-2x}(AlTi)_x$ was prepared by arc-melting a mixture of constituent elements with purities > 99.9 wt.%. Increasing Al and Ti additions enhanced the chemical driving force for the formation of $L1_2$ precipitates and promoted the destabilization of supersaturated FCC into $L1_2$ and σ phases. A high-strength rolled $(CoCrNi)_{94}Al_3Ti_3$ was hardened by nanoscale $L1_2$-(Ni, Co, Cr)$_3$(Ti, Al)-type particles with mixed heterogeneous and homogeneous precipitation behavior[22]. $(CoCrNi)_{94}Al_3Ti_3$ was

produced by arc-melting a mixture of high-purity raw elements. Incoherent σ-precipitates and a large number of coherent $L1_2$-precipitates were formed in rolled $(CoCrNi)_{94}Al_3Ti_3$, which enhanced the YS and UTS up to 1431 and 1683 MPa, respectively[23]. An ingot of the $(CoCrNi)_{94}Ti_3Al_3$ alloy was prepared by melting high purity elements. Dual heterogeneous nanostructures composed of heterogeneous partially recrystallized structure and heterogeneous $L1_2$ precipitates play a predominant role on the strengthening effect of rolled MEAs (Co:34.46, Cr:32.12, Ni:27.42 with Al:3, Ti:3 [in at.%])[24]. $(CoCrNi)_{94}Ti_3Al_3$ exhibited multiscale heterogeneous structures that contained favorable heterogeneous FCC matrix grains and coherent spherical γ′ nano-precipitates. A YS of 772 MPa and a ductility of 30.7% were achieved in laser powder bed fusion (L-PBF) $(CoCrNi)_{94}Al_3Ti_3$ MEA, where $(CoCrNi)_{94}Al_3Ti_3$ was prepared using pre-alloyed powders[19]. The high initial dislocation density and the segregation of Ti at the boundaries of cellular structures contributed to its high strength. The high performance of L-PBF $(CoCrNi)_{94}Al_3Ti_3$ MEA is attributed to the hierarchical microstructure with a high degree of heterogeneity in terms of grain size, cellular substructure, and characteristics of nano-precipitates ($L1_2$ phase)[18].

The requirements for the strength and plasticity of engineering materials in extreme environments are increasingly stringent. Thus, one of the most pressing problems is how to achieve enhanced strength and plasticity of engineering materials. The addition of small amounts of Al and Ti elements can remarkable enhance the strength of CoCrNi MEA, especially 3 at.% Al and 3 at.% Ti added to the CoCrNi matrix, which exhibited superior performance [22-24]. At present, pure metal arc-melting and pre-alloyed powders are the two major methods of Ti and Al addition. However, less research was performed on the strengthening mechanism of samples fabricated by mixed powders composed of TiAl and CoCrNi alloy powders, especially adopting direct L-DED. In the present work, the microstructure and mechanical properties of CoCrNi MEA doped with TiAl alloy were systematically investigated by L-DED. The strengthening and toughening mechanism of CoCrNi MEA was explored, and theoretical and practical references were provided for the design and fabrication of high-strength and plasticity alloys.

2. Experimental

The $(CoCrNi)_{94}(TiAl)_6$ MEA additive part was fabricated using a commercial L-DED system (TruLaser Cell 3000) equipped with a 4000 W coaxial powder feeding fiber laser. CoCrNi [iso-atomic ratio of Co (at.%):Cr (at.%):Ni (at.%) = 1:1:1] MEA powders and TiAl [iso-atomic ratio of Ti (at.%):Al (at.%) = 1:1] powders were mixed as the initial powders for L-DED. The total atomic ratio of CoCrNi in L-DED powder was 94%, and that of TiAl was 6%. The powders were fabricated using Ar atomization with dimensions ranging from 33 μm to 133 μm. The base plate was a mild steel with dimensions of 20 × 100 × 100 mm^3. The laser power, laser spot diameter, overlapping rate, and scanning velocity were 930 W, 1.7 mm, 50%, and 9 mm/s, respectively. Raster scan strategy was adopted with scanning direction rotated by 90° between the adjacent layers (Fig. 1a). The $(CoCrNi)_{94}(TiAl)_6$ MEA additive part (30 × 30 × 8 mm^3) is shown in Fig. 1b. The elemental distribution of $(CoCrNi)_{94}(TiAl)_6$ mixed powders is shown in Figs. 1c–h. A small amount of Ti and Al was detected in the powder. The XRD results showed that the TiAl powder had a tetragonal structure (Fig. 1i). Fig. 1j shows the XRD results of the $(CoCrNi)_{94}(TiAl)_6$ additive part. The microstructure was composed of single-phase FCC structure. The mechanical properties of the additive parts were tested at 298 and 77 K by using the UTM4304CD SUNS electronic universal testing machine. Electron backscatter diffraction (EBSD) was conducted using a field-emission scanning electron microscope (ZEISS Gemini SEM 300). The etching reagent used in the experiments consisted of 5 g $CuCl_2$, 100 mL HCl, and 100 ml ethanol. A TEM specimen was obtained by ion beam thinning. TEM was performed on an FEI Talos F200X TEM/scanning TEM (STEM) operated at 200 kV.

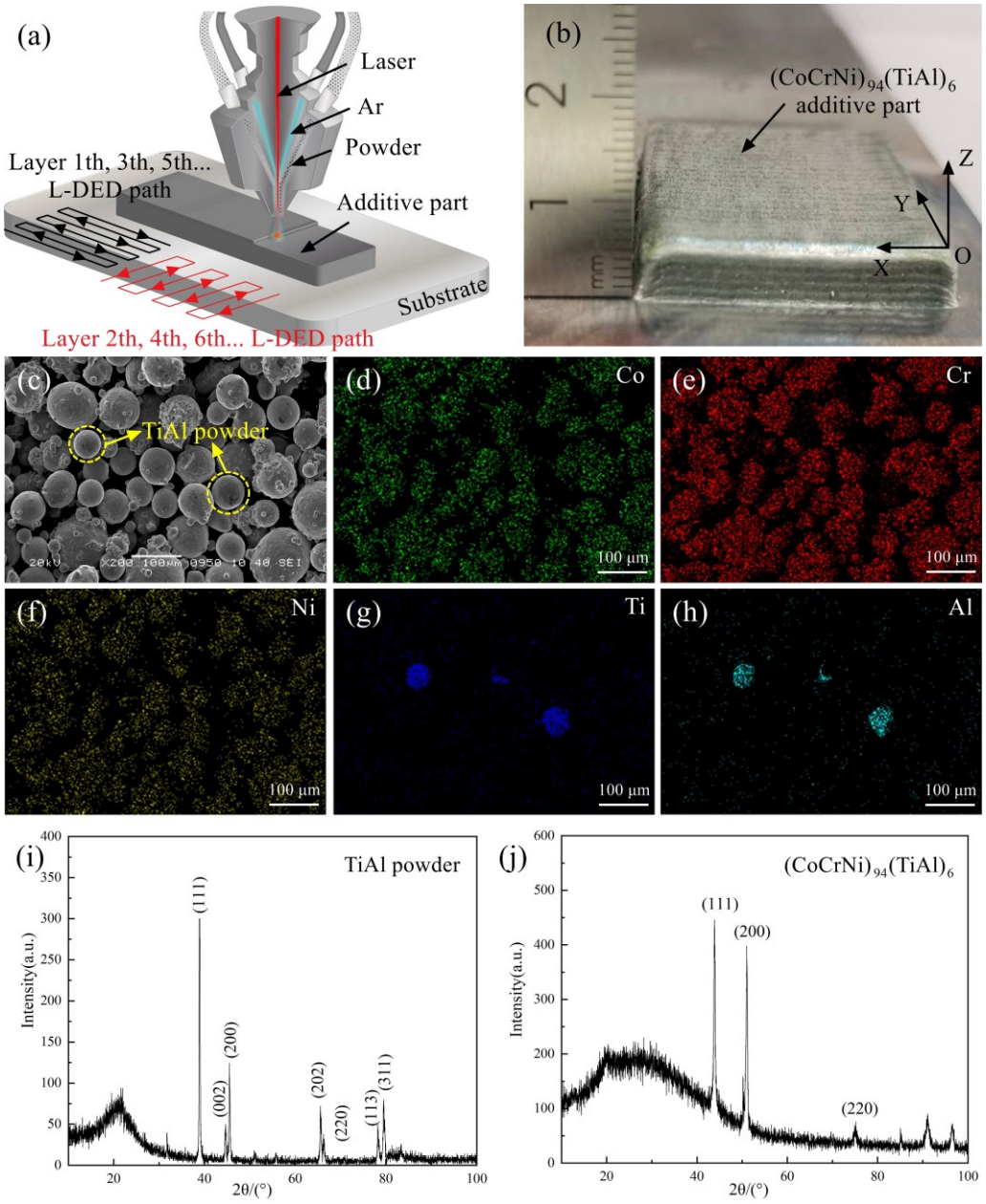

Fig. 1 Schematic diagram of $(CoCrNi)_{94}(TiAl)_6$ MEA additive manufacturing. (a) Laser direct energy deposited process, (b) $(CoCrNi)_{94}(TiAl)_6$ additive part, (c) $(CoCrNi)_{94}(TiAl)_6$ powder, (d)-(h) The distribution of Co, Cr, Ni, Ti and Al elements in $(CoCrNi)_{94}(TiAl)_6$ powder, (i)-(j) XRD of TiAl powder and $(CoCrNi)_{94}(TiAl)_6$ additive parts.

3. Results and discussion

3.1 Microstructure and mechanical properties for $(CoCrNi)_{94}(TiAl)_6$ additive parts

Adding alloying elements to powders is an important means for improving the properties of additive parts. The microstructures of the CoCrNi additive parts before and after the addition

of alloying elements are given in Fig. 2. Figs. 2a and 2b show the microstructures of the XOY and XOZ planes in the CoCrNi additive parts. A large number of columnar grains were found in the microstructure of both planes. The area containing columnar grains growing along the same direction was larger, and the size of the columnar grains varied widely. Previous results[25] showed that the average tensile strength and elongation in the XOY plane of the additive parts were 710.5 MPa and 48.8%, respectively. Meanwhile, the average tensile strength and elongation in the XOZ plane of the additive parts were 609.2 MPa and 101.0%, respectively. The additive parts showed significant anisotropy in the XOY and XOZ planes. Figs. 2c and 2d show the microstructures of both planes in the $(CoCrNi)_{94}(TiAl)_6$ additive parts. The microstructure of the $(CoCrNi)_{94}(TiAl)_6$ additive parts significantly differed from that of the CoCrNi additive parts. First, the volume of columnar grains decreased significantly, and only a small part of regions in the XOY plane included columnar grains, about 7.3%. Second, the grain diameter was smaller. Lastly, the grains changed from the initial columnar grains with uniform growth direction to fine dendrites. In addition, the columnar grains in the XOZ plane became finer, and the dimension difference of the columnar grains decreased.

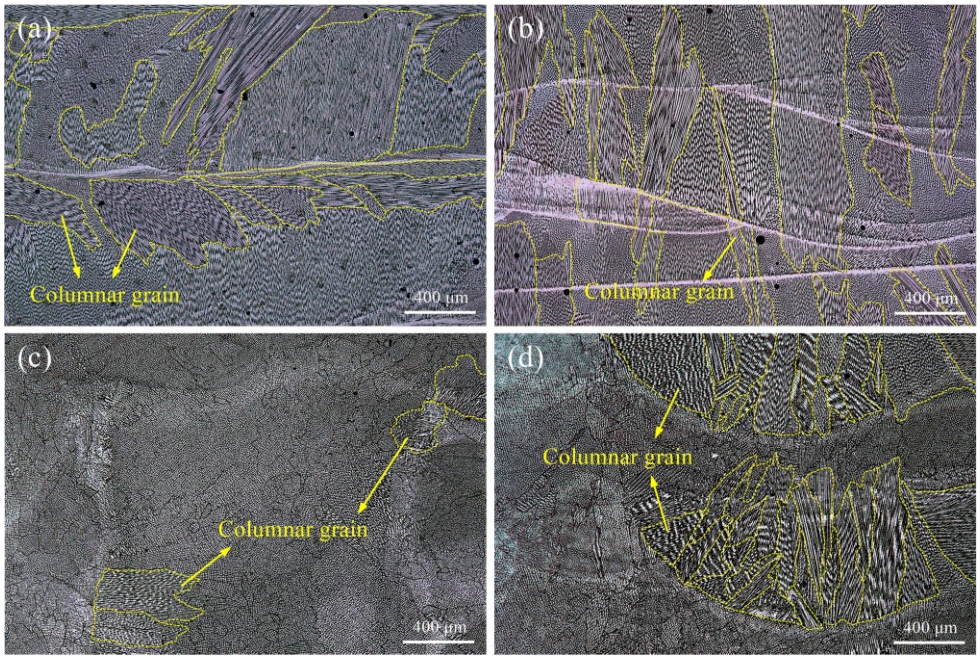

Fig. 2 The microstructure of MEA additive parts. (a) CoCrNi in XOY plane, (b) CoCrNi in XOZ plane, (c) $(CoCrNi)_{94}(TiAl)_6$ in XOY plane, (d) $(CoCrNi)_{94}(TiAl)_6$ in XOZ plane.

EBSD was used to analyze the microstructure of the additive parts to further investigate the difference between the microstructure of XOY and XOZ planes, as shown in Fig. 3. The inverse

pole figure (IPF), grain boundary distribution, kernel average misorientation (KAM), microstructure distribution, and pole figure (PF) of the $(CoCrNi)_{94}(TiAl)_6$ additive parts were determined. The IPF results (Figs. 3a and 3f) show that the colors in the different grains were relatively random, and no obvious orientation was found in the grains. Similarly, no obvious orientation was found in the larger and smaller size grains. The PF in Figs. 3b and 3g showed that the texture intensities of the XOY and XOZ planes were 6.13 and 18.19, respectively. These results clearly showed that the texture in the XOZ plane was stronger than that in the XOY plane. Figs. 3c and 3h show the results of sub-structured, recrystallization, and deformation microstructural distribution in the XOY and XOZ planes. Sub-structured, recrystallization, and deformation zones were found in the XOY plane, with volumes of 9.5%, 2.8%, and 87.7%, respectively. Meanwhile, the sub-structured, recrystallization and deformation zones in the XOY plane had volumes of 4.6%, 51.1%, and 44.3%, respectively. This finding indicated that recrystallization emerged continuously in the XOZ plane by thermal cycling, and more recrystallization occurred in the XOZ plane than in the XOY plane. As shown in Figs. 3d and i, the 2°–5° (red solid line) low-angle grain boundaries (LAGBs), 5°–15° (green solid line) LAGBs, and 15°–180° (blue solid line) high-angle grain boundaries (HAGBs) were counted. The grain boundaries of the larger-size grains were mainly colored green and blue, which indicated that the grain boundary angle was above 5°. Meanwhile, the fine grains were mainly dominated by 2°–5° LAGBs. The grain boundary angles in the sub-structured zone were mainly concentrated in the range of 5°–180°. As for the grains in the recrystallized zone, most of the grain boundary angles were in the range of 5°–15°, and a few were in the range of 5°–180°. By contrast, the grains in the deformed zone contained grain boundaries with all angles. Figs. 3e and 3j show the KAM of the $(CoCrNi)_{94}(TiAl)_6$ additive parts in the XOY and XOZ planes. High strain was found in the LAGBs and HAGBs.

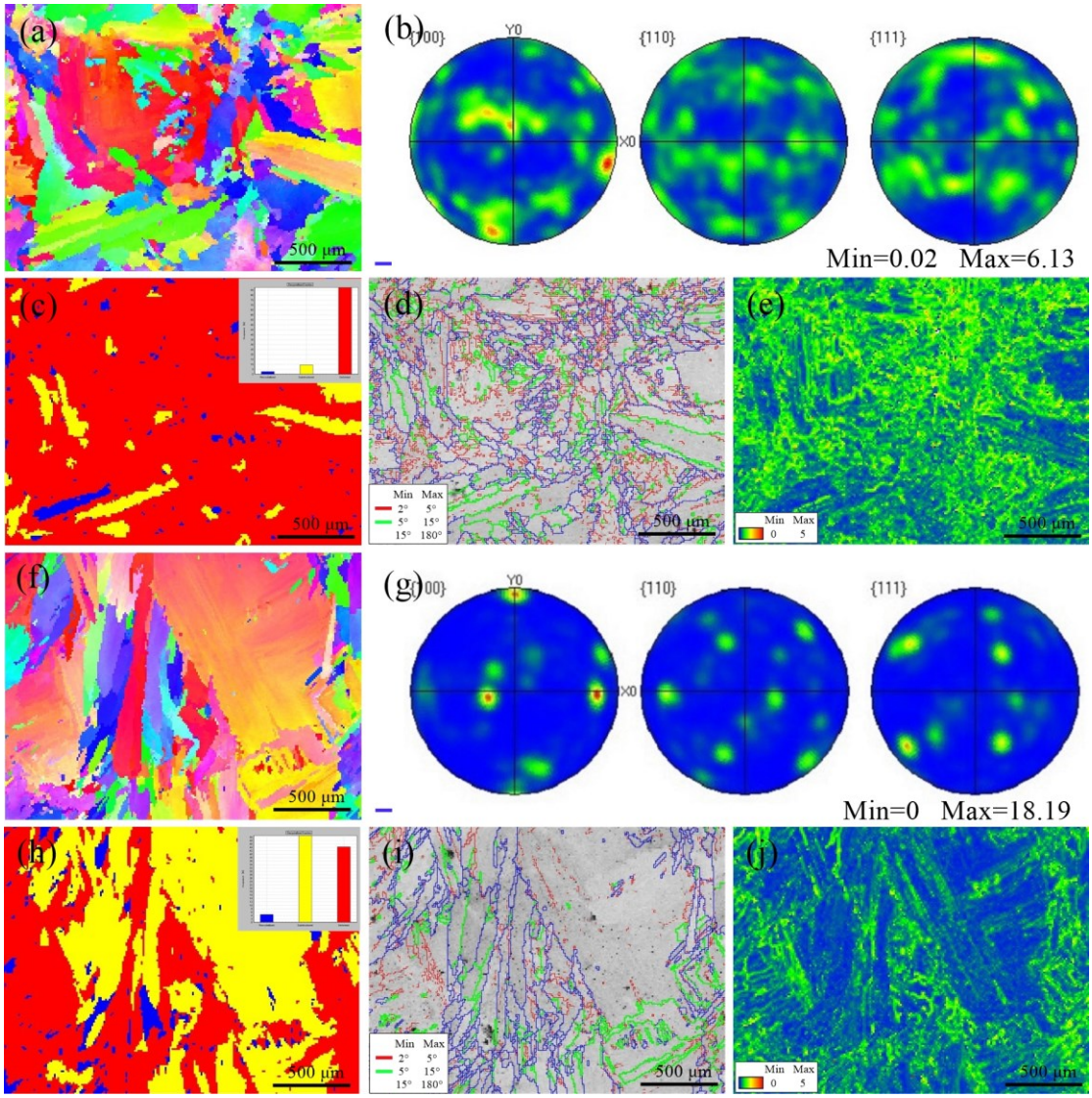

Fig.3 EBSD analysis for $(CoCrNi)_{94}(TiAl)_6$ additive parts in XOY and XOZ plane. (a) and (f) IPF-XOY and IPF-XOZ, (b) and (g) PF-XOY and PF-XOZ, (c) and (h) Substructured, recrystallization and deformation microstructure distribution in XOY and XOZ plane, (d) and (i) Grain boundary distribution in XOY and XOZ plane, (e) and (j) KAM-XOY and KAM-XOZ.

Fig. 4 shows the backscattered electron images of the $(CoCrNi)_{94}(TiAl)_6$ additive part with a large number of nano-precipitates in the microstructure. The CoCrNi matrix was brighter in color, whereas the nano-precipitates exhibited a dark black color. This finding indicated that the nano-precipitates may consist of one or both elements of Ti and Al. Scanning line analysis of the nano-precipitates was performed, and the results are shown in Figs. 4b–h. The whole scanning line results were divided into three parts: matrix region, Ti-enriched region, and Al-O-enriched region. In L-DED, air (O) is easily involved in the protecting atmosphere. In addition, obtaining pure powders without O is difficult. Previous studies found that O was

introduced into CoCrNi additive part to some extent[1]. The nano-precipitates consisted of an internal Al-O close to 1 μm in diameter and an external ring-like Ti compound. A partial overlap can be observed between the Al-O-enriched and Ti-enriched regions. In addition, the amount of Co, Cr, and Ni elements in the precipitated phase decreased.

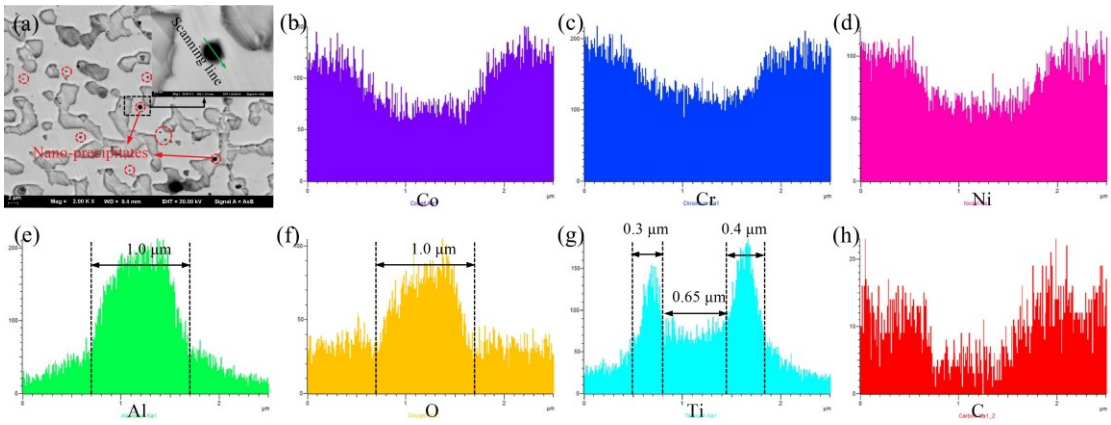

Fig. 4 The BSE images and scanning line results of $(CoCrNi)_{94}(TiAl)_6$ additive parts. (a) BSE; (b)-(f) scanning line results of Co, Cr, Ni, Al, O, Ti and C elements in Fig. 4a.

A single-phase FCC structure is the primary matrix in CoCrNi additive parts. When a small amount of TiAl was added to CoCrNi, the microstructure changed significantly. Besides the finer grains obtained, a large number of fine nano-precipitates were found in the microstructure. STEM was used to investigate the influence of nano-precipitates on the property enhancement of the $(CoCrNi)_{94}(TiAl)_6$ additive parts. Fig. 5a shows a bright field image of the TEM sample, and the typical morphology of the nano-precipitates was clearly visible. The interface between the nano-precipitates and the matrix demonstrated a flatter boundary. Furthermore, the nano-precipitates presented a polygonal morphology. Elemental and selected area electron diffraction (SAED) was performed on the nano-precipitates to explore the composition and structure of the precipitated phase, as shown in Figs. 5a–i. The compositions of the matrix P1 and nano-precipitates P2 and P3 were $Co_{34.0}Cr_{29.0}Ni_{30.5}Ti_{2.3}O_{4.2}$ (at.%), $Co_{3.6}Cr_{1.3}Ni_{1.0}Ti_{94.1}$ (at.%), and $Co_{2.8}Cr_{3.1}Ni_{1.9}Ti_{2.3}Al_{89.9}$ (at.%), respectively. The elemental distribution results showed that the matrix was mainly composed of CoCrNi elements, and the nano-precipitates were a core–shell structure mainly made up of Ti-based alloy externally and Al-based alloy internally. A small amount of Al was detected in the matrix and Ti-based alloy, even though 3 at.% Al was added to the matrix. The maximum solubility of Co, Cr, Ni, and Al in α-Ti were about 0.98 at.%[26],

0.35 at.%[27], 10 at.%[28], and 21.6 at.%[29], respectively. Given the limited solubility of Co, Cr, Ni, and Al in Ti, SEAD was performed for the Ti-based alloy region, as shown in Fig. 5i. The lattice parameters of Ti could not be matched by calibrating the diffraction spot. The Ti-based alloy may be composed of Ti-C or Ti-O compounds when considering the inaccuracy of O and C contents found in STEM. The diffraction spot was analyzed and identified as an FCC structure, which indicated that the Ti-based alloy region was composed of TiO.

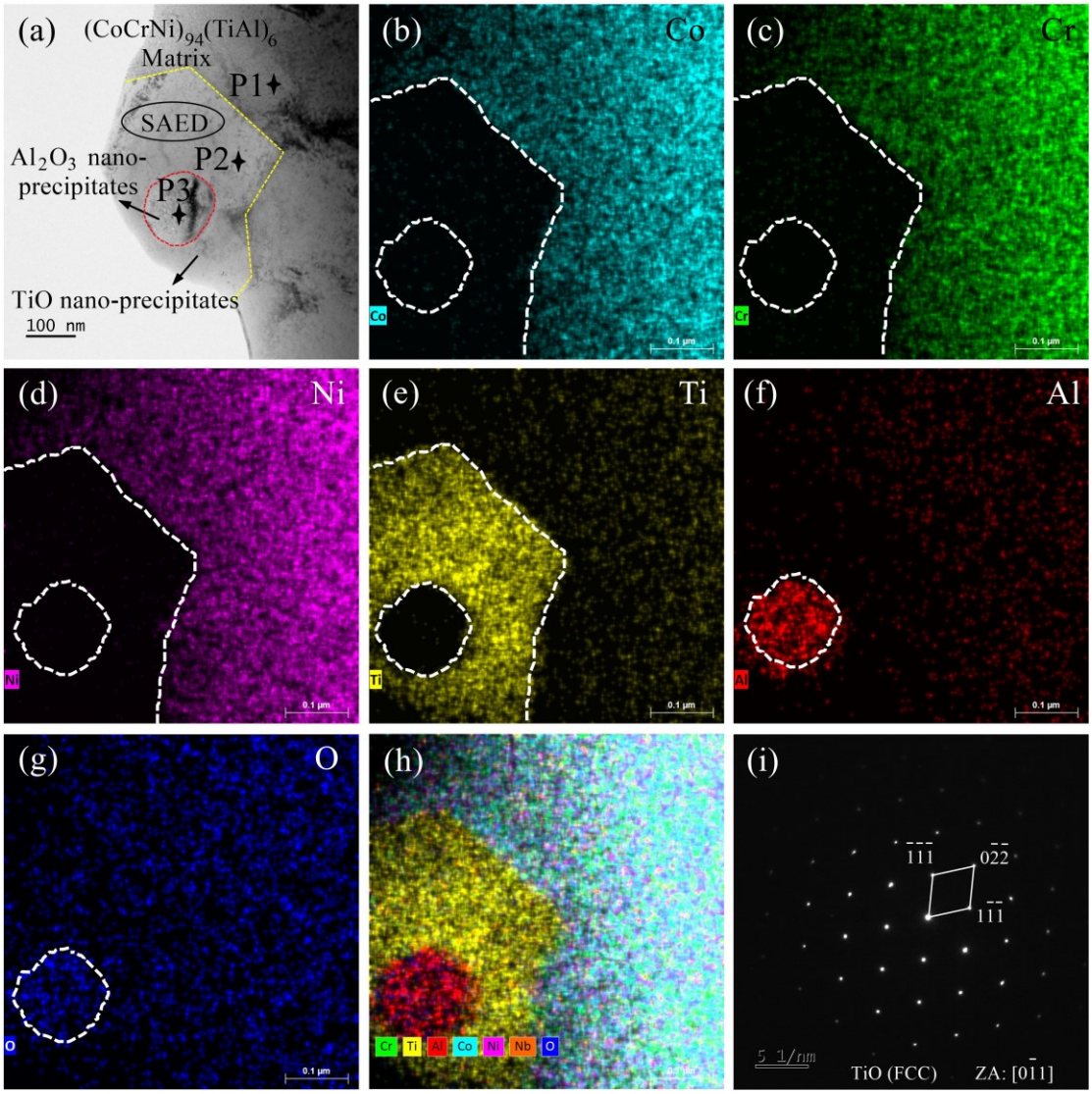

Fig.5 TEM analysis results of $(CoCrNi)_{94}(TiAl)_6$ additive parts. (a) Bright field image; (b)-(g) Co, Cr, Ni, Ti, Al and O elements mapping results. (h) Elemental distribution group, (i) SAED in Fig.5a.

In response to Ti-O oxides, high-resolution images were used to analyze the TiO region and its vicinity, and the results are shown in Fig. 6. Figs. 6a and 6d present the high-resolution images of the matrix/TiO interface and matrix. Fast Fourier transform (FFT) was performed on the $(CoCrNi)_{94}(TiAl)_6$ matrix. The FFT results showed that the matrix remained a single-phase

FCC structure, even though small amounts of Ti and O dissolved into the matrix. The lattice constant of the $(CoCrNi)_{94}(TiAl)_6$ matrix was calculated to be 3.66 Å. As for the TiO region near the matrix/TiO interface, its FFT and local magnification are shown in Figs. 6b and 6e. On the $(111)_{TiO}$ plane, its interplanar spacing was 2.500 Å, and the $(\bar{1}\bar{1}1)_{TiO}$ interplanar spacing was 2.494 Å, which were close to the TiO (FCC) theoretical value. The lattice constant of TiO was calculated to be 4.32 Å. The high-resolution images and local enlargements of the nano-precipitates composed of Al-based alloy inside are shown in Fig. 6c and 6f. A single-phase FCC structure was shown in the FFT results of the Al_2O_3 region. The lattice constant of Al_2O_3 was calculated to be 8.09 Å. The high-resolution image of the TiO region close to the TiO/Al_2O_3 interface is shown in Fig. 6g. The grain orientation of the TiO region close to the TiO/Al_2O_3 interface was the same as that of the TiO region close to the matrix/TiO interface, indicating a uniform orientation of TiO. Figs. 6h and i show the orientation relationships (ORs) of the matrix/TiO and TiO/Al_2O_3 interface. The matrix/TiO demonstrated the following ORs:

$$(020)_{matrix}/(111)_{TiO}: \angle 16.1°$$

$$(002)_{matrix}/(\bar{1}\bar{1}1)_{TiO}: \angle 3.8°$$

$$(022)_{matrix}/(002)_{TiO}: \angle 6.0°$$

Meanwhile, TiO/Al_2O_3 showed the following ORs:

$$(111)_{TiO}/(002)_{Al_2O_3}: \angle 13.9°$$

$$(\bar{1}\bar{1}1)_{TiO}/(11\bar{1})_{Al_2O_3}: \angle 1.7°$$

$$(002)_{TiO}/(111)_{Al_2O_3}: \angle 14.6°$$

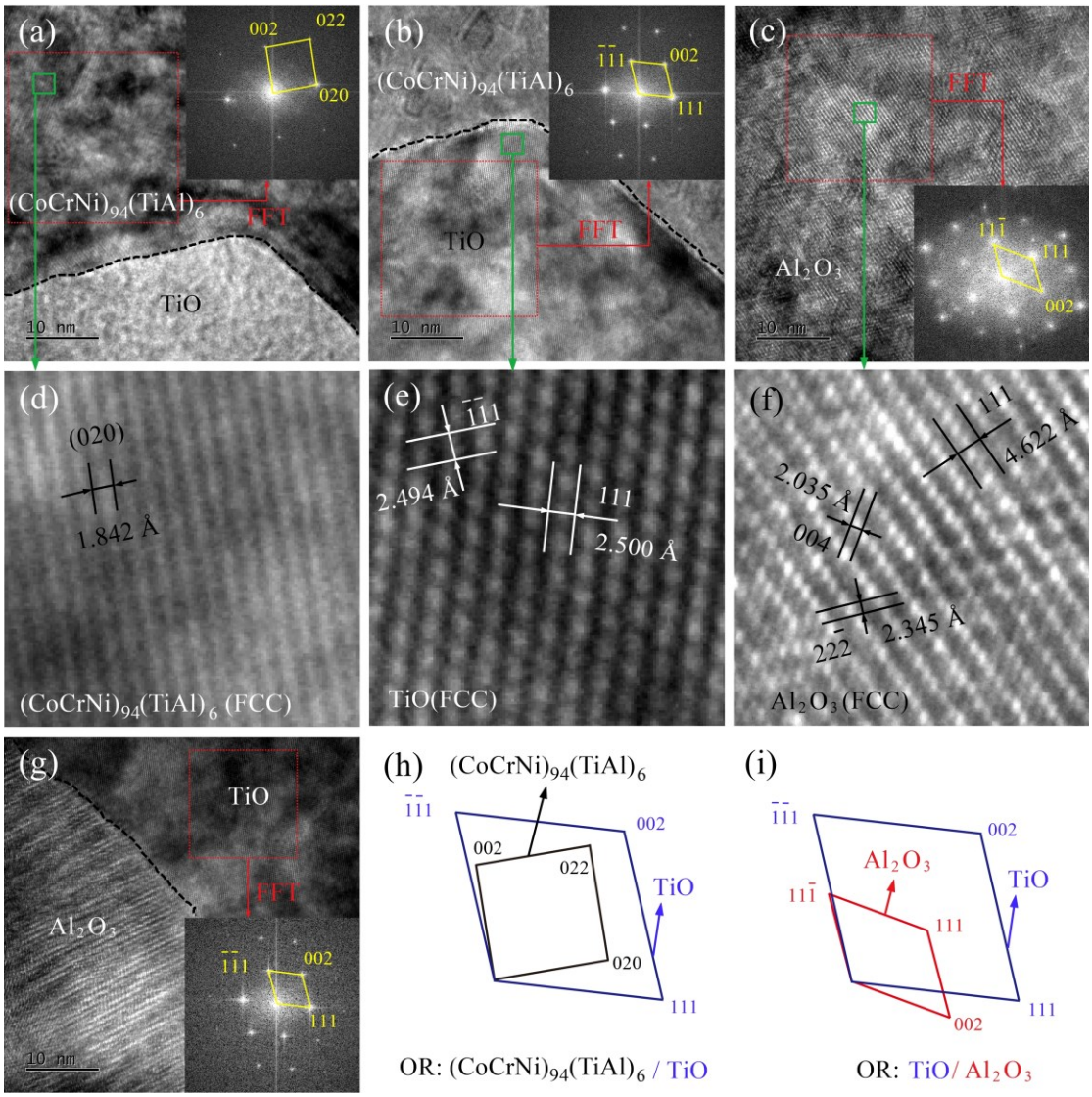

Fig. 6 High-resolution images of $(CoCrNi)_{94}(TiAl)_6$ additive parts. (a)-(b) Matrix/TiO interface, (c) Al_2O_3 region, (d) Enlarged view in Fig. 6a, (e) Enlarged view in Fig. 6b, (f) Enlarged view in Fig. 6c, (g) TiO/Al_2O_3 interface, (h)-(i) OR of matrix/TiO and TiO/Al_2O_3 interface.

The TEM results showed that the strength enhancement of the $(CoCrNi)_{94}(TiAl)_6$ additive parts was mainly due to the emergence of nano-precipitates in the microstructure. The nanoscale precipitates are functional to refine the grains and prevent dislocation motion and stacking fault (SF) expansion during the deformation process, and thus improve the properties of the additive parts. Precipitation strengthening is one of the important factors for the property improvement of $(CoCrNi)_{94}(TiAl)_6$ additive parts. The nano-precipitates had TiO clad Al_2O_3 core–shell structures, where the external is TiO with FCC structure and the internal is Al_2O_3 with FCC structure. Small amounts of Co, Cr, and Ni solidly dissolved in TiO, and small amounts of Co, Cr, Ni, and Ti solidly dissolved in the FCC structure of Al_2O_3. Therefore, establishing a growth

model of core–shell structures in $(CoCrNi)_{94}(TiAl)_6$ additive parts is important to elucidate their strengthening mechanism.

Fig. 7 shows the tensile data of CoCrNi and $(CoCrNi)_{94}(TiAl)_6$ additive parts at 298 and 77 K. The average tensile strength, YS, and elongation of the CoCrNi additive parts at 298 K were 692.8 MPa, 436.2 MPa, and 37.6%, respectively. When TiAl powder was added to the CoCrNi additive parts, a significant increase in tensile strength and YS was noticed. The average tensile strength and YS of the $(CoCrNi)_{94}(TiAl)_6$ additive parts at 298 K were 898.2 and 585.7 MPa, respectively, which were 29.6% and 34.3% higher than with those of the CoCrNi additive parts (Fig. 7a). However, the addition of TiAl reduced the elongation of the CoCrNi additive parts by 17.0%, indicating that the room-temperature properties of the $(CoCrNi)_{94}(TiAl)_6$ additive parts improved at the expense of plastic toughness. CoCrNi is known to exhibit higher properties at cryogenic temperatures, and the actual tensile results were consistent with this conclusion. The tensile strength, YS, and elongation of CoCrNi increased at cryogenic temperatures, with values of 988.6 MPa, 665.3 MPa, and 40.4%, respectively (Fig. 7b). Moreover, the cryogenic properties of the $(CoCrNi)_{94}(TiAl)_6$ additive parts enhanced in comparison with those of CoCrNi. The average tensile strength, YS, and elongation of the $(CoCrNi)_{94}(TiAl)_6$ additive parts at 77 K were 1251.5 MPa, 812.5 MPa, and 54.1%, respectively. Although the elongation of the $(CoCrNi)_{94}(TiAl)_6$ additive parts decreased at 298 K compared with that of CoCrNi, a higher elongation was achieved at cryogenic temperatures.

The typical engineering stress–strain curves of CoCrNi and $(CoCrNi)_{94}(TiAl)_6$ additive parts at 298 and 77 K are shown in Fig. 7c. Both additive parts exhibited a rapid increase in stress, with a strain less than 1% at 298 K. The mechanical properties of the additive parts grew slowly when the strain increased below 1% at 77 K. The stress lied in the rapid growth rate when the strain was in the range of 1%–8%, indicating that cryogenic temperature induces a greater plastic potential in CoCrNi-based MEAs. These results showed that the strength of the $(CoCrNi)_{94}(TiAl)_6$ additive parts can be improved by nano-precipitate toughening. However, the plasticity of the additive parts can decrease at 298 K. No crystallographic orientation was observed between the nano-precipitates and the matrix, and the dislocation line cannot slice the nano-precipitates. Therefore, the dislocation line bypasses the nano-precipitates during the plastic deformation of the alloy.

Fig. 7d shows the strain hardening rate curve of the CoCrNi and $(CoCrNi)_{94}(TiAl)_6$ additive parts. The strain hardening rates at 298 and 77 K exhibited different hardening characteristics. The strain hardening rate of the CoCrNi additive parts at 298 K demonstrated two stages: an initial sharp decrease and a smooth decrease in the second stage until fracture. Meanwhile, the strain hardening rate of the $(CoCrNi)_{94}(TiAl)_6$ additive parts at 298 K was characterized by four stages: an initial sharp decrease, a brief increase followed by a rapid decrease in the second stage, a smooth transition accompanied by a slight increase in the third stage, and fracture of the specimen in the fourth stage. The increase in strain hardening rate in the second and third stages was caused by severe plastic deformation inducing dislocation pile-up near the nano-precipitates. The hardening rate curve at cryogenic temperature was slightly different from that at room temperature. The strain hardening rate of the CoCrNi additive parts at cryogenic temperatures showed three stages: an increase, a decrease, and a steady decrease until fracture. Meanwhile, the strain hardening rate of the $(CoCrNi)_{94}(TiAl)_6$ additive parts had four stages: an increase, a decrease, a smooth transition accompanied by a slight increase, and fracture. The difference is that in the third stage, the CoCrNi strain hardening rate decreased slightly, whereas the $(CoCrNi)_{94}(TiAl)_6$ strain hardening rate increased slightly. The increase in strain hardening rate that occurred in the first stage at cryogenic temperatures is due to the fact that low SF energy can lead to the formation of more SFs and induce higher plasticity. The increase in $(CoCrNi)_{94}(TiAl)_6$ strain hardening rate in the third stage is due to a combination of dislocation pile-up near the nano-precipitates, harmonized deformation of the nano-precipitates and matrix, and the generation of twinning-induced plasticity effects in the matrix.

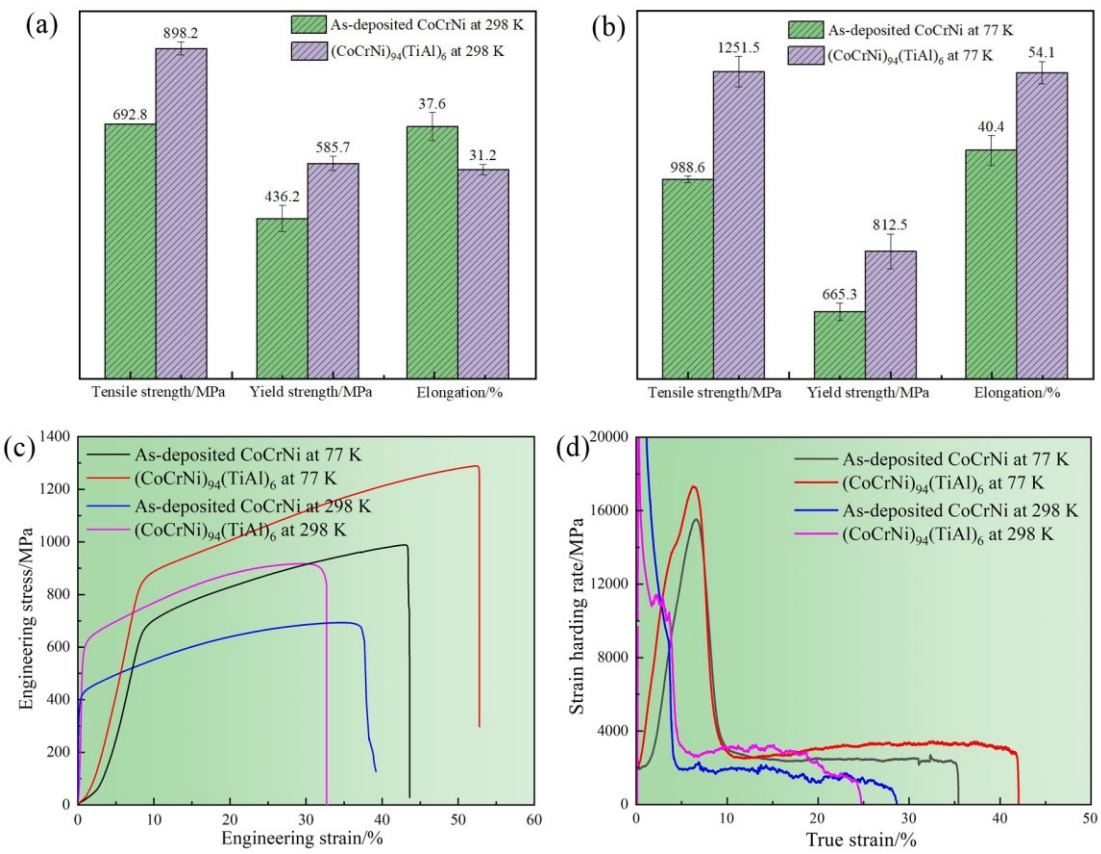

Fig. 7 Mechanical properties of as-deposited CoCrNi and $(CoCrNi)_{94}(TiAl)_6$ additive parts. (a) Mechanical properties at 298 K, (b) Mechanical properties at 77 K, (c) The engineering stress-engineering strain curves, (d) Variation in strain hardening rates.

3.2 Nano-precipitate strengthening mechanism in $(CoCrNi)_{94}(TiAl)_6$ additive parts

STEM was performed to observe the structure and compositions of the $(CoCrNi)_{94}(TiAl)_6$ additive parts, especially the OR between the nano-precipitates and the matrix. TEM was performed on the tensile specimens to evaluate the deformation of the $(CoCrNi)_{94}(TiAl)_6$ additive parts under large deformation conditions to illustrate their strengthening mechanism. Figs. 8a–c show bright-field images of the TEM specimens of the $(CoCrNi)_{94}(TiAl)_6$ additive parts. As shown in Figs. 8a and 8b, the edges of the nano-precipitates were flatter, and their core–shell structure was made up of TiO externally and Al_2O_3 internally. A large number of dislocations appeared around the nano-precipitates, and the dislocations were entangled with one another. In addition, more SFs were found in the non-dislocation tangle (DT) region (Fig. 8a). Besides cross-slip, DT and SFs can be found in Fig. 8b. The emergence of cross-slip enabled $(CoCrNi)_{94}(TiAl)_6$ with better uniform deformability and higher strength. Fig. 8c shows the bright-field image of the matrix, which showed DT. Together with the dislocation and SF

interactions, the strength of the additive part improved. Fig. 8d shows the high-angle annular dark field (HAADF) of the nano-precipitates after deformation, and the nano-precipitates were mainly a core–shell structure. The subsequent EDS results (Figs. 8e and 8f) indicated that the nano-precipitates consisted of Al_2O_3 inside and TiO outside, and the matrix was mainly composed of CoCrNi.

In comparison with the properties of the CoCrNi additive part without TiAl, those of the $(CoCrNi)_{94}(TiAl)_6$ additive parts improved considerably, and the tensile strength increased by 205.4 MPa at 298 K. The high-resolution images of the tensile specimens of the $(CoCrNi)_{94}(TiAl)_6$ additive parts were observed to explore the strengthening mechanism, as shown in Figs. 8g–l. Fig. 8g shows the high-resolution image of the matrix, where a large number of SFs were observed. Combined with the FFT results, the SFs clearly extended mostly along the $(111)_{matrix}$ plane and a few along the $(\bar{1}1\bar{1})_{matrix}$ plane. A local enlarged view of the SFs in the matrix is shown in Fig. 8h, and the widths of the SFs were 1.715 and 2.798 nm, respectively. Similarly, high-resolution observation (Fig. 8j) of the matrix/TiO interface was carried out, and a large number of SFs were found in the matrix region, close to the nano-precipitates. The SFs extended along the $(111)_{matrix}$ and $(\bar{1}1\bar{1})_{matrix}$ planes, and some of the SFs crossed to form Lomer–Cottrell (L–C) locks. The high-resolution images of the region close to the boundary of the nano-precipitates are illustrated in Fig. 8k, where the SFs terminated in the matrix close to the nano-precipitate boundary. An SF terminal region of about 2 nm width was found at the location where the SF terminated from the nano-precipitate boundary. Inverse FFT (IFFT) was performed on a set of symmetric diffraction spot $(110)_{matrix}$ planes, as shown in Figs. 8i and 8l. The higher dislocation density close to the nano-precipitates was higher than that in the matrix, indicating that the nano-precipitates contributed to the increased level of DT.

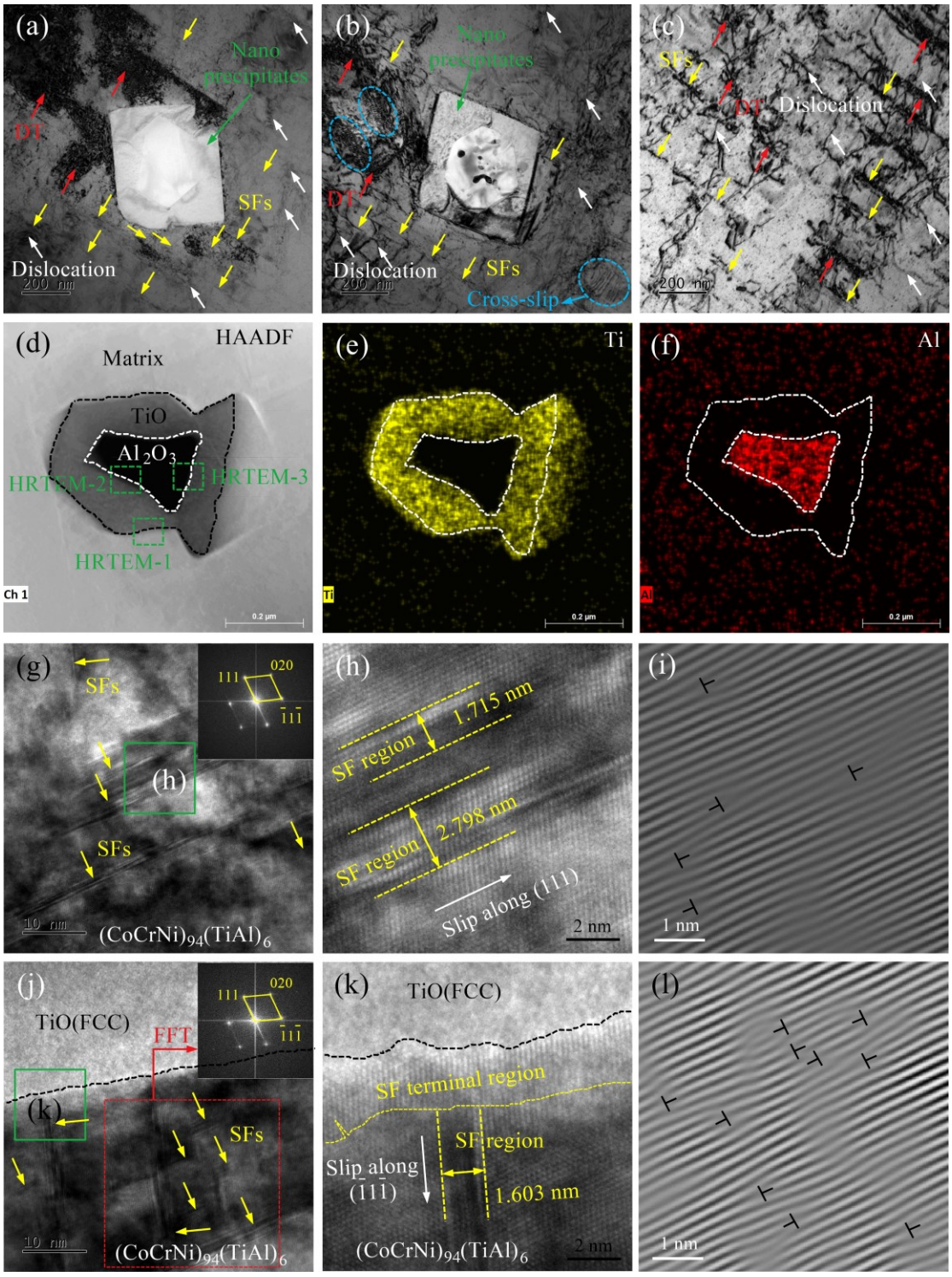

Fig. 8 TEM analysis results of $(CoCrNi)_{94}(TiAl)_6$ tensile samples at 298 K. (a)-(b) Bright field image of nano-precipitates, (c) Bright field image of matrix, (d) HAADF of nano-precipitates, (e)-(f) Ti and Al elements mapping results of nano-precipitates, (g) High-resolution image of matrix, (h) Enlarged view in Fig. 8g, (i) IFFT along $(111)_{matrix}$ plane, (j) High-resolution image of HRTEM-1 in Fig. 8d, (k) Enlarged view in Fig. 8j, (l) IFFT along $(111)_{matrix}$.

Figs. 9a and 9d show the high-resolution images of the TiO/Al_2O_3 interface at two locations

(HRTEM-2 and HRTEM-3 in Fig. 8d). No SFs were found in the TiO and Al_2O_3 regions when observing their high-resolution images (Figs. 9a and 9d). Figs. 9b and 9c show the IFFT along the $(\bar{2}02)_{Al_2O_3}$ plane and $(220)_{TiO}$ planes, respectively. Some dislocations were detected in the TiO and Al_2O_3 regions at the HRTEM-2 location. Meanwhile, no dislocation was found in the Al_2O_3 regions at the HRTEM-3 location, whereas dislocations were found in the TiO regions. This finding indicated that dislocation motion and SF extension were the principal deformation mechanisms of the $(CoCrNi)_{94}(TiAl)_6$ matrix during the deformation process. Dislocations in nano-precipitates were formed during the plastic deformation process. As for the FCC structure of Al_2O_3, which was inside TiO, a partial region showed deformation. Therefore, the nano-precipitates mainly plays a role in impeding dislocation motion, splitting layer dislocations, and inducing cross-slip generation, thus contributing to the strength improvement of the additive parts. Figs. 9a and 9d present the FFT results for TiO and Al_2O_3. The FFT results showed that the matrix/TiO had the following ORs:

$$(\bar{1}1\bar{1})_{matrix}/(202)_{TiO}: \angle 9.8°$$

$$(111)_{matrix}/(0\bar{2}2)_{TiO}: \angle 20.4°$$

$$(020)_{matrix}/(220)_{TiO}: \angle 15.4°$$

Meanwhile, the TiO/Al_2O_3 had the following ORs:

$$(202)_{TiO}/(103)_{Al_2O_3}: \angle 0.8°$$

$$(02\bar{2})_{TiO}/(\bar{3}0\bar{1})_{Al_2O_3}: \angle 1.3°$$

$$(220)_{TiO}/(\bar{2}02)_{Al_2O_3}: \angle 1.3°$$

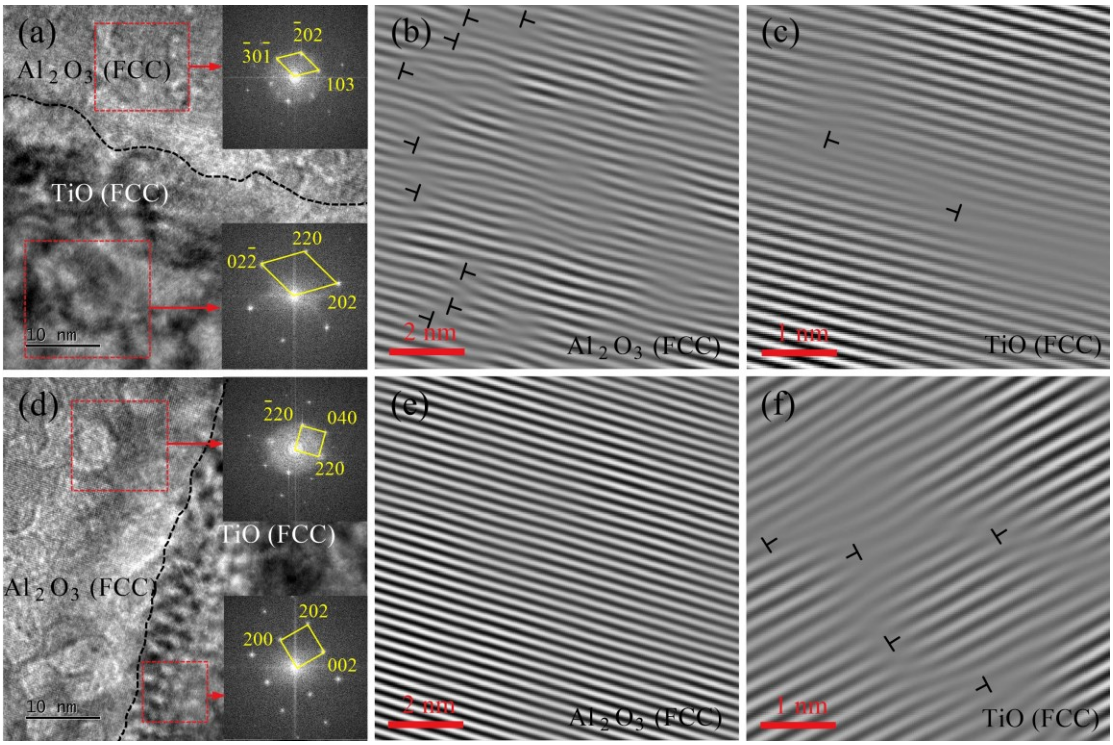

Fig. 9 High-resolution images of nano-precipitates in $(CoCrNi)_{94}(TiAl)_6$ tensile samples at 298 K. (a) HRTEM-2 in Fig. 8d, (b) IFFT along $(\bar{2}02)_{Al_2O_3}$ plane, (c) IFFT along $(220)_{TiO}$ plane, (d) HRTEM-3 in Fig. 8d, (e) IFFT along $(\bar{2}20)_{Al_2O_3}$ plane, (f) IFFT along $(200)_{TiO}$ plane.

Taking into account that the CoCrNi additive parts exhibited better properties at cryogenic temperatures, the deformation mechanism at 77 K was more expected. Fig. 10 shows the high-resolution images of $(CoCrNi)_{94}(TiAl)_6$ tensile samples at 77 K. Compared with the TEM morphology at 298 K, the dislocation density in the matrix increased at 77 K (Fig. 10a). Meanwhile, the high-resolution images of the matrix were analyzed, as shown in Fig. 10b. The SF density in the matrix clearly increased, and twinning occurred in some areas. The width of the twinning was about 5 nm. SFs were observed around the twinning boundary (TB) and in the twinning. A large number of nano-precipitates appeared in the matrix, and their TEM morphology under 77 K tensile is shown in Fig. 10c. Numerous dislocations were wrapped around the nano-precipitates. Fig. 10d shows the high-resolution image of the matrix/TiO interface. SFs clearly appeared in the matrix, whereas no SFs were found in the TiO region. The FFT results of the matrix and TiO near the matrix/TiO interface are shown in Figs. 10e and g. The orientation of the matrix and TiO was consistent. The matrix/TiO interface had the following ORs: $(111)_{matrix}//(111)_{TiO}$, $(\bar{1}\bar{1}1)_{matrix}//(\bar{1}\bar{1}1)_{TiO}$, and $(002)_{matrix}//(002)_{TiO}$. The IFFT results of the matrix and TiO (111) plane diffraction spots are shown in Figs. 10f and 10h. A

large number of dislocations occurred in the matrix, whereas only a small number of dislocations occurred in the TiO region. Similar findings were shown in the matrix/TiO interface (Fig. 10i). The orientation of the Al_2O_3 region in the interior of the nano-precipitates was consistent with that of the TiO region in the exterior (Fig. 10j). The TiO/Al_2O_3 interface demonstrated the following ORs: $(111)_{TiO}//(111)_{Al_2O_3}$, $(\bar{1}\bar{1}1)_{TiO}//(\bar{1}\bar{1}1)_{Al_2O_3}$, and $(002)_{TiO}//(002)_{Al_2O_3}$. Dislocations were also detected in the Al_2O_3 region (Fig. 10k) and TiO/Al_2O_3 interface (Fig. 10l). This finding indicated that plastic deformation at cryogenic temperature resulted in synergistic deformation of the nano-precipitates and matrix, and the orientation of the deformed nano-precipitates was consistent with that of the matrix.

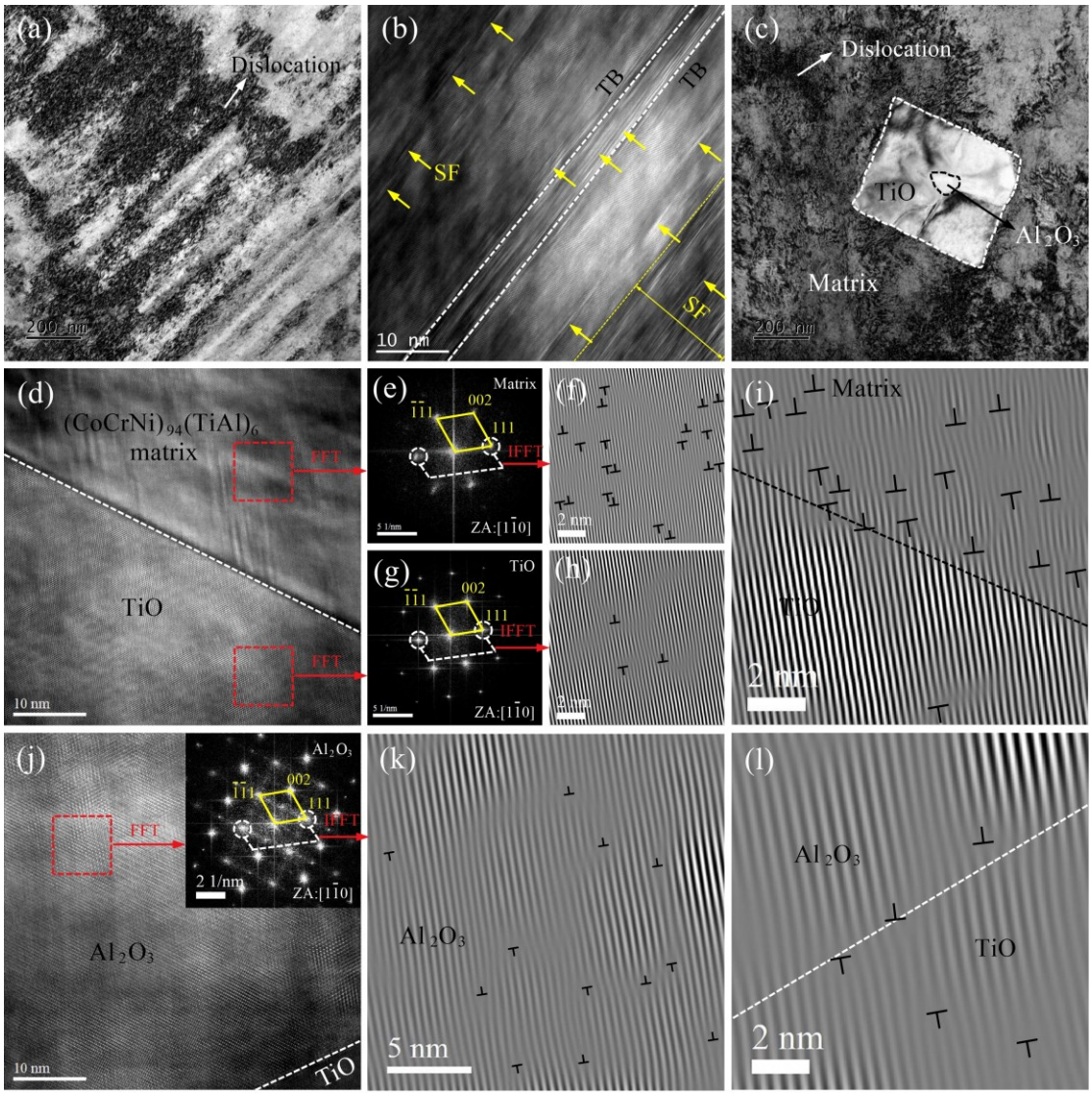

Fig. 10 High-resolution images of matrix and nano-precipitates in $(CoCrNi)_{94}(TiAl)_6$ tensile samples at 77 K. (a) Bright field image of matrix, (b) High-resolution image of matrix, (c) Bright field image of nano-precipitates, (d) High-resolution image of matrix/TiO interface, (e) FFT of Matrix; (f) IFFT along

$(111)_{matrix}$ plane, (g) FFT of TiO; (h) IFFT along $(111)_{TiO}$ plane, (i) IFFT of matrix/TiO interface, (j) High-resolution image of TiO/Al_2O_3 interface, (k) IFFT along $(111)_{Al_2O_3}$ plane, (l) IFFT of TiO/Al_2O_3 interface.

3.3 Growth model of core–shell structures in $(CoCrNi)_{94}(TiAl)_6$ additive parts

Fig. 11 illustrates the different morphologies of the nano-precipitates and their composition. A small number of circular (Fig. 11a) and fan-shaped nano-precipitates (Fig. 11b) appeared in the matrix. The elemental scanning results (Figs. 11e, 11i, and 11m) showed that the circular structure was mainly composed of Al. The diffraction spot calibration results indicated that the circular structure was Al_2O_3. Few TiO existed around Al_2O_3. The fan-shaped structure of the nano-precipitates was different from the circular structure, which was mainly composed of Ti (Figs. 11f, 11j, and 11n). The Ti-enriched region in the fan-shaped nano-precipitates was mainly composed of TiO. A small amount of Al aggregated inside the fan-shaped nano-precipitates, verified to be Al_2O_3. However, most of the nano-precipitates were polygonal structures, as shown in Figs. 11c and d. The polygonal structures were core–shell structures (Figs. 11g and 11h, 11k and 11l, and 11o and 11p) composed of Al_2O_3 internally and TiO externally. The Al_2O_3 in the polygonal structure was larger in size than that in the fan-shaped structure. Most of the Al_2O_3 in the nano-precipitates were circular or polygonal.

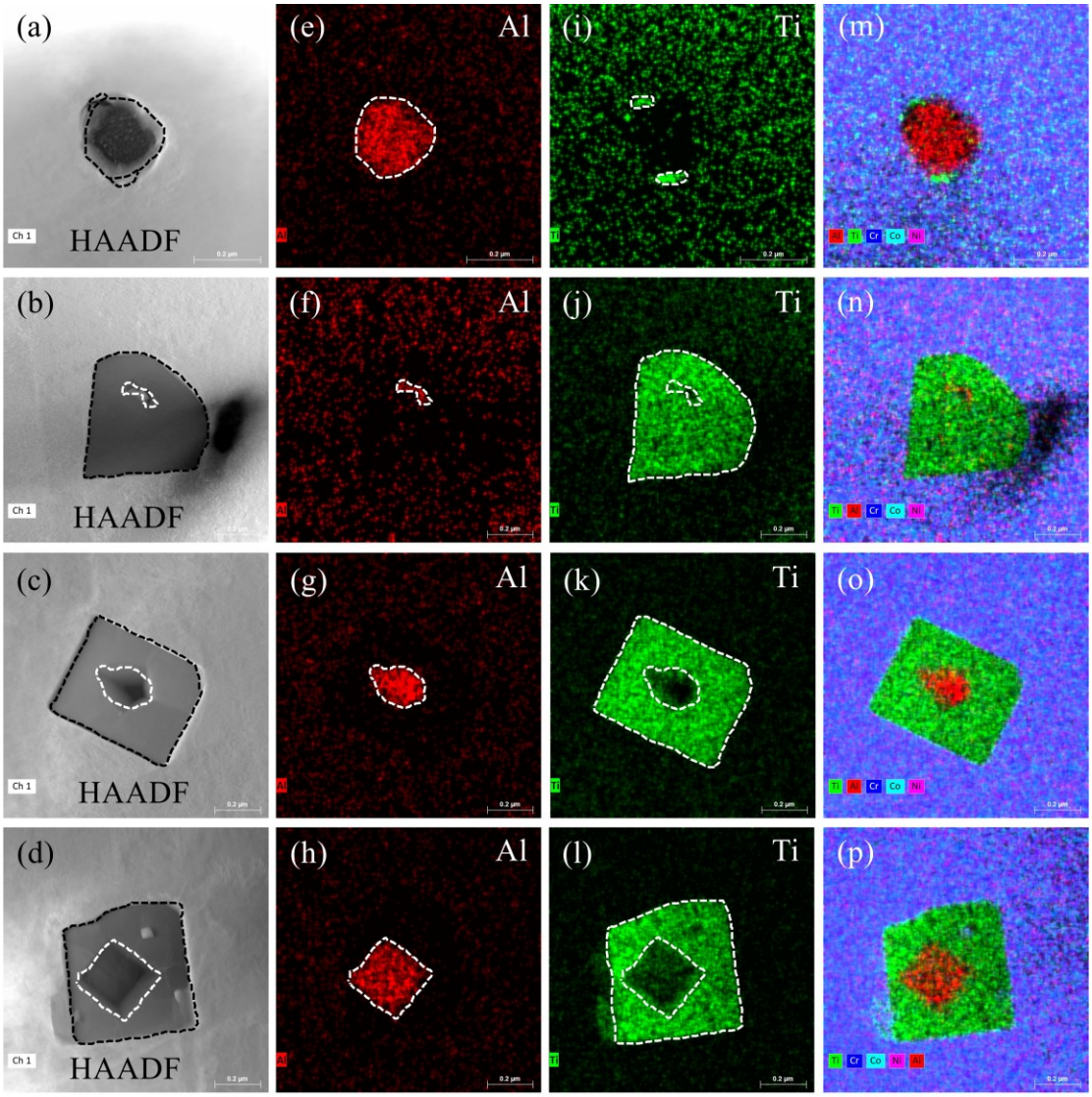

Fig. 11 Nano-precipitates morphology and compositional analysis results. (a)-(d) HAADF of nano-precipitates, (e)-(h) Al element distribution, (i)-(l) Ti element distribution, (m)-(p) Elemental distribution group.

The growth model of core–shell structures in the $(CoCrNi)_{94}(TiAl)_6$ additive parts is shown in Fig. 12. When TiAl powders were added to the CoCrNi matrix and melted by laser, Al-Ti-Ni-enriched phase predominantly generated in the matrix, and a new core–shell structured nano-precipitates appeared. Considering that the enthalpy of mixing of Al-Ti is smaller than that of Al-Co, Al-Cr, and Al-Ni, the TiAl powders remained agglomerated after melting. During L-DED, the O in the environment and powder may lead to the formation of oxide nano-precipitates with core–shell structure [1]. The O element in the matrix gradually approached the melted Ti-Al region, and the Ti-Al-O aggregation zone finally formed. When the temperature of the fusion zone dropped to the melting point of Al_2O_3 (2345 K), Al_2O_3 was

preferentially precipitated from the liquid phase. As the fusion zone kept cooling, liquid Ti atoms gathered around Al_2O_3. When the fusion zone temperature dropped to the melting point of TiO (2023 K), Ti and O reacted to form TiO, which encapsulated Al_2O_3. When the fusion zone temperature dropped to the melting point of CoCrNi alloy (1718 K), the matrix began to solidify. During the whole solidification process, small amounts of Co, Cr, Ni, and Ti were solidly dissolved in Al_2O_3 with the diffusion of atoms. These elements took the place of the Al atoms and eventually formed an Al_2O_3-based solid solution. Moreover, small amounts of Co, Cr, and Ni were solidly dissolved in TiO, leading to the formation of a TiO-based solid solution. Considering the stronger adsorption of O to Al, most of the Al was consumed by O. Thus, only a small amount of Ti and O was solidly dissolved in the matrix.

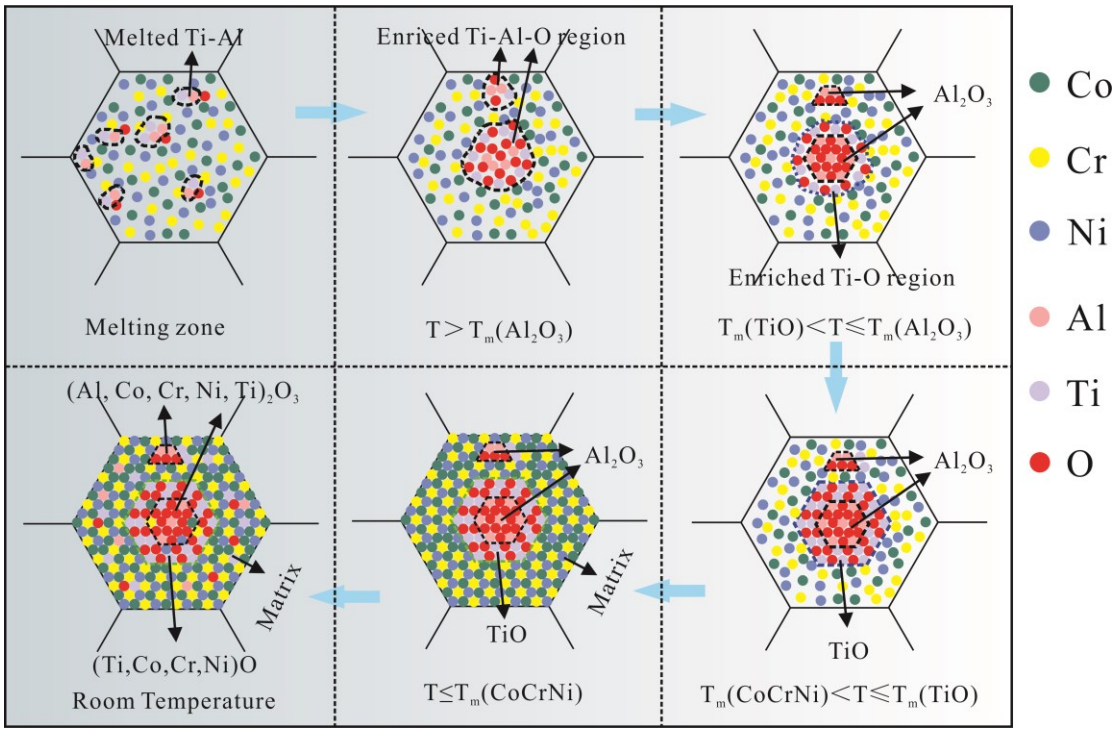

Fig. 12 Growth model of core-shell structures in $(CoCrNi)_{94}(TiAl)_6$ additive parts.

4. Conclusions

This study provides a detailed investigation of the strengthening induction mechanism in $(CoCrNi)_{94}(TiAl)_6$ laser-directed energy deposition additive part. On the basis of the results of SEM, EBSD, STEM, and HRTEM characterizations, the main findings were summarized as follows:

(1) The microstructure of the $(CoCrNi)_{94}(TiAl)_6$ additive parts is significantly different from that of the CoCrNi additive parts. The grains in the CoCrNi additive parts change from the initial columnar grains with uniform growth direction to fine dendrites in $(CoCrNi)_{94}(TiAl)_6$ additive parts. Sub-structured, recrystallization, and deformation zones can be found in the XOY plane, with volumes of 9.5%, 2.8%, and 87.7%, respectively. Meanwhile, the volumes of sub-structured, recrystallization, and deformation zones in the XOY plane are 4.6%, 51.1%, and 44.3%, respectively.

(2) The average tensile strength, yield strength and elongation of the CoCrNi additive parts at 298 K were 692.8 MPa, 436.2 MPa and 37.6%, while 898.2 MPa, 585.7 MPa and 31.2% obtained after TiAl added. The average tensile strength, yield strength and elongation of the CoCrNi additive parts at 77 K were 988.6 MPa, 665.3 MPa and 40.4%, while 1251.5 MPa，812.5 MPa and 54.1% obtained after TiAl added.

(3) The nano-precipitates are functional to refine the grains and prevent the dislocation motion and SF expansion during the deformation process, thus improving the properties of the additive parts. The matrix is mainly composed of CoCrNi elements, whereas most nano-precipitates are core–shell structures mainly made up of TiO externally and Al_2O_3 internally.

(4) $(CoCrNi)_{94}(TiAl)_6$/TiO has the following ORs: $(020)_{matrix}//(111)_{TiO}$, ∠ 16.1°; $(002)_{matrix}//(\bar{1}\bar{1}1)_{TiO}$, ∠3.8°; and $(022)_{matrix}//(002)_{TiO}$, ∠6.0°. Meanwhile, TiO/$Al_2O_3$ has the following ORs: $(111)_{TiO}//(002)_{Al_2O_3}$, ∠13.9°; $(\bar{1}\bar{1}1)_{TiO}//(11\bar{1})_{Al_2O_3}$, ∠1.7°; and $(002)_{TiO}//(111)_{Al_2O_3}$: ∠14.6°. No crystallographic orientation can be found between the nano-precipitates and the matrix, and the dislocation line cannot slice the nano-precipitates.

(5) The SFs extended along the (111) and $(\bar{1}1\bar{1})$ planes after tensile test, and some of the SFs crossed to form L–C locks. An SF terminal region of about 2 nm width was found at the location where the SF terminated from the nano-precipitate boundary. The dislocation line bypassed the nano-precipitates during the plastic deformation of the alloy, which induces further strengthening of the $(CoCrNi)_{94}(TiAl)_6$ additive parts.

(6) Plastic deformation at cryogenic temperature resulted in synergistic deformation of the nano-precipitates and matrix, and the orientation of the deformed nano-precipitates was consistent with that of the matrix. The matrix/TiO interface has the following ORs: $(111)_{matrix}//(111)_{TiO}$, $(\bar{1}\bar{1}1)_{matrix}//(\bar{1}\bar{1}1)_{TiO}$, and $(002)_{matrix}//(002)_{TiO}$. The TiO/$Al_2O_3$ interface has

the following ORs: $(111)_{TiO}//(111)_{Al_2O_3}$, $(\bar{1}\bar{1}1)_{TiO}//(\bar{1}\bar{1}1)_{Al_2O_3}$, and $(002)_{TiO}//(002)_{Al_2O_3}$.

Declaration of Competing Interest

The authors declare that they have no known competing financial interests or personal relationships that could have appeared to influence the work reported in this paper.

Acknowledgements

This work was supported by the National Natural Science Foundation of China (No. 52075228, 52075317 & 51971144), National Key R&D Program of China (No. 2022YFB46021022), the Natural Science Foundation of the Higher Education Institutions of Jiangsu Province (No. 20KJ430001) and Jiangsu Province Graduate Research Innovation Plan (KYCX22_3786).

References:

[1] Bi X, Li R, Li T, Zhang X, Cheng J, Tian Y. Cracks suppression strategies for CoCrNi medium entropy alloy fabricated by laser directed energy deposition. MATER DESIGN 2023;226:111579.

[2] Bi X, Li R, Li T, Liu B, Yuan Y, Zhang P, Feng K. Anisotropic microstructure, properties and molecular dynamics simulation of CoCrNi medium entropy alloy fabricated by laser directed energy deposition. Materials Science and Engineering: A 2023;871:144834.

[3] Lu W, Luo X, Yang Y, Zhang J, Huang B. Effects of Al addition on structural evolution and mechanical properties of the CrCoNi medium-entropy alloy. MATER CHEM PHYS 2019;238:121841.

[4] Kim H, Lee D, Kim H, Kim Y, Jang M, Kwen D, Koo Y, Kim E, Cho H, Agustianingrum MP. The formation of B2-precipitate and its effect on grain growth behavior in aluminum-containing CoCrNi medium-entropy alloy. MATER LETT 2021;303:130481.

[5] Lee D, Jeong H, Lee K, Jeon JB, Park N. Precipitation and grain-boundary strengthening of Al-added CoCrNi medium-entropy alloys. MATER LETT 2019;250:127.

[6] Zheng M, Li C, Zhang X, Ye Z, Liao Y, Gu J. Design of a novel (CoCrNi)84.5Al15.5 eutectic medium-entropy alloy with hierarchically nano-lamellar microstructure through additively manufactured compositionally graded materials. Materials Science and Engineering: A 2023:145209.

[7] Liu X, Zhang M, Ma Y, Dong W, Li R, Lu Y, Zhang Y, Yu P, Gao Y, Li G. Achieving ultrahigh strength in CoCrNi-based medium-entropy alloys with synergistic strengthening effect. Materials Science and Engineering: A 2020;776:139028.

[8] Chang R, Fang W, Yan J, Yu H, Bai X, Li J, Wang S, Zheng S, Yin F. Microstructure and mechanical properties of CoCrNi-Mo medium entropy alloys: Experiments and first-principle calculations. J MATER SCI TECHNOL 2021;62:25.

[9] Wang J, Yang H, Huang H, Ruan J, Ji S. In-situ Mo nanoparticles strengthened CoCrNi medium entropy alloy. J ALLOY COMPD 2019;798:576.

[10] Chen H, Li D, Geng Z, Wu Y, Zhang T, Jiang X, Zhao S, Zhang H, Han Y, Liu X, Chen C. Additive manufactured high-strength tungsten composite with high deformability by using a novel CoCrNi medium-entropy binder. Composites Part B: Engineering 2022;246:110256.

[11] Chang R, Fang W, Bai X, Xia C, Zhang X, Yu H, Liu B, Yin F. Effects of tungsten additions on the microstructure and mechanical properties of CoCrNi medium entropy alloys. J ALLOY COMPD 2019;790:732.

[12] Pan Z, Luo H, Wei Y, Cheng H, Wang X, Zhao Q, Li X. Segregation of solute elements and strengthening effects of CoCrNiCux medium-entropy alloys: A combined experimental and simulation study. J ALLOY COMPD 2023;941:169015.

[13] Jodi DE, Park N. Phase separation and its effect on atomic interactions in CoCrNiCux medium-entropy alloys. MATER LETT 2019;255:126528.

[14] Feng X, Surjadi JU, Fan R, Li X, Zhou W, Zhao S, Lu Y. Microalloyed medium-entropy alloy (MEA) composite nanolattices with ultrahigh toughness and cyclability. MATER TODAY 2021;42:10.

[15] Zheng M, Li C, Ye Z, Zhang X, Yang X, Wang Q, Gu J. Strength-ductility synergy of additively manufactured (CoCrNi)87Al13 medium entropy alloy with heterogeneous multiphase microstructure. SCRIPTA MATER 2023;222:115016.

[16] Shen P, Liu H, Huang C, Yen H, Yeh J, Tsai C. Microstructure and mechanical properties of medium-entropy alloys with a high-density η-D024 phase. MATER CHARACT 2022;185:111713.

[17] Liu XS, Li R, Li AX, Xu S, Yang H, Yu SB, Jiang MH, Huo C, Yu PF, Wang YY, Li G. A novel high-strength and high-ductility CoCrNi medium entropy alloy by Ti/Mo co-doping. MATER LETT 2022;326:132929.
[18] Yao N, Lu T, Feng K, Sun B, Wang R, Wang J, Xie Y, Zhao P, Han B, Zhang X. Ultrastrong and ductile additively manufactured precipitation-hardening medium-entropy alloy at ambient and cryogenic temperatures. ACTA MATER 2022;236:118142.
[19] Li Z, Zhao P, Lu T, Feng K, Tong Y, Sun B, Yao N, Xie Y, Han B, Zhang X, Tu S. Effects of post annealing on the microstructure, precipitation behavior, and mechanical property of a (CoCrNi)94Al3Ti3 medium-entropy alloy fabricated by laser powder bed fusion. J MATER SCI TECHNOL 2023;135:142.
[20] Wang J, Zou J, Yang H, Dong X, Cao P, Liao X, Liu Z, Ji S. Ultrastrong and ductile (CoCrNi)94Ti3Al3 medium-entropy alloys via introducing multi-scale heterogeneous structures. J MATER SCI TECHNOL 2023;135:241.
[21] Fang J, Liu WH, Luan JH, Jiao ZB. Phase stability and precipitation in L12-strengthened CoCrNi medium-entropy alloys at intermediate temperatures. J PHASE EQUILIB DIFF 2021;42:781.
[22] Zhao YL, Yang T, Tong Y, Wang J, Luan JH, Jiao ZB, Chen D, Yang Y, Hu A, Liu CT, Kai JJ. Heterogeneous precipitation behavior and stacking-fault-mediated deformation in a CoCrNi-based medium-entropy alloy. ACTA MATER 2017;138:72.
[23] Yi H, Wei D, Xie R, Zhang Y, Kato H. A strategy for enhancing the mechanical property of the precipitation-strengthened medium-entropy alloy. Materials Science and Engineering: A 2021;819:141390.
[24] Du XH, Li WP, Chang HT, Yang T, Duan GS, Wu BL, Huang JC, Chen FR, Liu CT, Chuang WS. Dual heterogeneous structures lead to ultrahigh strength and uniform ductility in a Co-Cr-Ni medium-entropy alloy. NAT COMMUN 2020;11:2390.
[25] Bi X, Li R, Li T, Liu B, Yuan Y, Zhang P, Feng K. Anisotropic microstructure, properties and molecular dynamics simulation of CoCrNi medium entropy alloy fabricated by laser directed energy deposition. Materials Science and Engineering: A 2023;871:144834.
[26] Straumal BB, Korneva A, Kilmametov AR, Lityńska-Dobrzyńska L, Gornakova AS, Chulist R, Karpov MI, Zięba P. Structural and mechanical properties of Ti – Co alloys treated by high pressure torsion. MATERIALS 2019;12:426.
[27] Katsuyoshi K, Ryuho I, Junko U, Shota K, Khantachawana A. Microstructural and mechanical properties of α-titanium sintered material via thermal decomposition of additive chromium oxide particles. Materials Science and Engineering: A 2019;739:491.
[28] Semenova EL, Krendelsberger NY. Alloy structures of the Ti-Ni-Ru system in the Ti-TiNi-TiRu composition range. Platinum Metals Review 2001;45:84.
[29] Kornilov II, Pylaeva EN, Volkova MA. Phase diagram of the binary system titanium-aluminum. Bulletin of the Academy of Sciences of the USSR, Division of chemical science 1956;5:787.